Word Count: 8128

REVIEW 2

Fluorine behavior during experimental muscovite dehydration melting and natural partitioning between micas: Implications for the petrogenesis of peraluminous leucogranites and pegmatites

RICARDO SALLET[1], JONATHAN D. PRICE[2], CARLOS RIBEIRO[3], MARIA HELENA B. M. HOLLANDA[4], ISAAC J. SAYEG[4], AND DANIEL HARLOV[5,6,7]

[1]Departamento de Geologia, Universidade Federal do Rio Grande do Norte, UFRN, Campus Universitário, 59078-900, Natal, RN, Brazil

[2] Kimbell School of Geosciences, Midwestern State University, 3410, Taft Blvd. Wichita Falls, TX, 76308, USA

[3]Instituto de Geociências, Universidade de Brasília, UnB, Campus Universitário Darcy Ribeiro, 70910-900, Brasília, DF, Brazil

[4]Instituto de Geociências, Universidade de São Paulo, USP, Butantã, 05508-080, São Paulo, SP, Brazil

[5]Deutsches GeoForschungsZentrum – GFZ, Telegrafenberg, 14473 Potsdam, Germany

[6]Department of Geology, University of Johannesburg P.O. Box 524, Auckland Park, 2006 South Africa

[7]Faculty of Earth Resources, China University of Geosciences, 430074 Wuhan, China

ABSTRACT

Fluorine behavior during the partial melting of two-mica bearing protoliths have been experimentally investigated at 700 to 930 °C and 0.4 and 0.6 GPa. Muscovite dehydration and H_2O-HF fluid assisted partial melting experiments were carried out using both a natural and synthetic two-mica schist made of natural micas. The mineral composition of the experiments was assessed by BSE imaging and EDS analyses. The F, Cl and major elements contents of the glass and micas were determined by EPMA.

The muscovite dehydration melting reaction is muscovite + quartz + plagioclase = peraluminous melt + biotite + sillimanite + potassic feldspar ± hercynite. The starting biotite stays largely stable showing only minor melt + ilmenite and trace magnetite formation in the cleavages. The neo-formed biotite shows similar F contents and a slightly higher X_{Sid} component when compared to the starting biotite. HF-added experiments yield F-rich neo-formed biotite.

The obtained melts consisted of a peraluminous leucogranite with F contents increasing with F-rich protoliths. The bulk partition coefficient $D_F^{\ schist/melt}$ increases from 0.5 to 3.0 when the F content of the protolith rises from 0.05 to 1.2 wt%. The partition coefficient, $Kd_F^{\ Bt/melt}$, increases from 2.0 to 6.0 where the biotite MgO content increases from 5 to 18 wt%. The natural partition coefficient $Kd_F^{Bt/Ms}$, measured for a set of rocks with a varied lithology from the Seridó Belt, NE, Brazil, was 2.7 ± 0.5.

The obtained F partition coefficients, along with published F partition coefficients, between biotite and melt, biotite and muscovite, and fluid and melt, allow for the modeling of F behavior during muscovite dehydration and fluid-present melting. F-rich, two-mica protoliths will increase F partitioning in favor of the micaceous anatectic residue compared

to the peraluminous melt. Furthermore, the model indicates that the more Fe-rich the schist and its residual biotite are, the higher the F content of the melt and the fluid. Fluorine-rich peraluminous leucogranites and related fluids may be generated by the anatexis of F- and Fe-rich, two-mica protoliths. As F can be a complexing ligand for Li, Be, Cs, Nb, Ta, W, Sn, and U, muscovite dehydration could potentially be associated with metallic occurrences associated with peraluminous melts.

Keywords: anatexis, peraluminous leucogranite, micas, fluid, fluorine partition

INTRODUCTION

The anatexis of Al-rich rocks within the continental crust produces peraluminous melts forming leucogranitic plutons (e.g., Nabelek 2022) and pegmatitic vein fields (e.g., Wise et al. 2022). The partially melted continental crust form migmatites where the anatectic granitic melt crystallize as a leucosome network along with a residual refractory mineral assembly or melanosome, usually bearing neo-formed or peritectic phases (e.g., Sawyer 2010). The mineralogical and chemical composition of the leuco- and melanosome are determined by the prevailing temperature and pressure, the presence of a fluid phase and its composition, and the chemical and mineralogical nature of the partially melted protolith (e.g., Gao et al. 2016; Sallet et al. 2015; Weinberg and Hasalovà 2015).

Theoretical and experimental findings point to three main anatectic processes that result in granitic melts within the continental crust: (i) fluid saturated partial melting, in the temperature range of 600 to 700 °C (e.g., Acosta-Vigil et al. 2006; Beard et al. 1994; Beard and Lofgren 1991; Carroll and Wyllie 1990; Gardien et al. 2000; Genier et al. 2008; Holtz

and Johannes 1991; Sallet et al. 2015; Sawyer 2010; Weinberg and Hasalovà 2015) (ii) fluid-absent muscovite dehydration melting in the temperature range of 650 to 750 °C (e.g., Anenburg and Katzir 2014; Brearley and Rubie 1990; Castro et al. 2000; Dyck et al. 2019; Gardien et al. 1995; Michaud et al. 2021; Patiño Douce and Harris 1998; Storre 1982) and (iii) fluid-absent biotite and amphibole dehydration melting at higher temperatures, in the range of 850 to 900 °C (e.g., Michaud et al. 2021; Patiño Douce and Beard 1995; Peterson et al. 1991; Pickering and Johnston 1998; Sallet et al. 2015; Skjerlie and Johnston 1993; Thompson 1982; 1996; Vielzeuf and Holloway 1988)

Fluid-absent melting reactions by dehydration of micas (and amphibole) implies a potential fractionated OH-F-Cl release from their hydroxyl site to the melt. Consequently, the residual and neo-formed hydroxyl bearing phases may acquire different OH-F-Cl compositions (e.g., Fink and Thompkins 2017; Hansen and Harlov 2007; Peterson et al. 1991; Pickering and Johnston 1998; Sallet et al. 2015, 2018). On the other hand, anatexis under fluid saturation by external influx at near eutectic temperatures may allow the micas to remain stable while quartz + feldspars experience partial melting (Weinberg and Hasalovà 2015, and references therein). In this case, anionic exchange with melt and fluid potentially modifies the mica OH-F-Cl composition by solid state inter-diffusion in the mica crystal lattice with the melt and/or the fluid as an F-Cl-OH source or sink (Sallet et al. 2018).

In this study, we experimentally investigated the geochemical behavior of F in peraluminous leucogranites and pegmatites (e.g., Nabelek 2019) during the anatexis of two-mica protoliths. ~~Attempts to characterize the Cl content yielded consistently low Cl contents near the detection limit of standard analytical methods (Sallet et al. 2015, 2019)~~. The experiments aimed to determine how F partitions between mica and melt during anatexis.

We also determined the partitioning of F between coexisting biotite and muscovite for a set of schist, granite, and pegmatitic granite samples (Sallet et al., 2018, 2021).

Along with previously published F partition coefficients (Icenhower and London 1997; Webster and Holloway 1990) our results allow for the modeling of the F composition of residual micas, melt, and fluid, if present, during the anatexis of two-mica bearing schists and peraluminous granites. The obtained results assessed anatexis at the origin of peraluminous granites and pegmatites and their associated fluids. Enrichment in Li, Be, Cs, Nb, Ta, W, Sn, and U are commonly associated with F-rich peraluminous leucogranitic melts and related fluids (e.g., Cuney et al. 2002; Harlaux et al. 2017; Linnen et al. 2012; Nabelek 2019). Metal enrichment of peraluminous leucogranitic melts, generated by muscovite dehydration melting, may be related to F and metal-rich muscovite-rich protoliths.

MATERIAL AND METHODS

Starting materials

In this study we used samples of mica schist, paragneiss, granite, and pegmatitic granite, along with their biotite and muscovite concentrates, all collected across the Seridó belt, Borborema Province, NE Brazil (Sallet et al. 2015, 2018, 2019). We crushed, divided, and ground sample aliquots for chemical analyses and for mica separation as starting materials for the experiments. We selected rock fragments for polished thin sections and epoxy plugs for petrographic and microanalysis. Biotite and muscovite concentrates were obtained from the schists using a Frantz electromagnetic separator at the University of Geneva, Switzerland.

Biotite and muscovite (1 to 5 cm in size) were separated out from the pegmatitic granites by hand-picking .

For partial melting experiments we selected as the natural starting material two rock samples, the F-rich, two-mica schist PPL18, and the F-poor, two-mica schist MLIM (Sallet et al. 2015, 2018, 2021) (Table 1). Both samples were collected from the contact of the Seridó schist with pegmatitic granite intrusions, where unoriented muscovite flakes have developed in the biotite schist. We also used a synthetic schist as a starting material, which consisted of a 51 wt% biotite + 34 wt% muscovite + 15 wt% synthetic quartz mixture (Table 1). The micas, selected from schists and pegmatitic granites, cover a wide range of F contents, from 0.1 to 2.3 wt% (Table 2). They include biotite and muscovite from the Seridó schist (PPL18 and MLIM), biotite from the regional Seridó biotite schist collected at the Santo André quarry (StAnd), biotite from meter-wide granitic pegmatite dykes (STAN and PBT1), muscovite from the Parelhas pegmatitic granite (PReg), and muscovite from the Alto do Sino zoned pegmatite (ASM) (Sallet et al. 2015, 2018, 2021).

We evaluated the F partitioning between the biotite and muscovite in a selected set of Seridó Belt natural samples, including the Seridó mica schist, the Jucurutu gneiss, the Acari granite, and the pegmatitic granites (Sallet et al. 2015, 2021).

Whole rock analysis

Whole rock chemical analyses of the major elements and F contents in the starting materials were determined at the SARM-CNRS, Nancy, France and ACME, Vancouver, Canada. The whole-rock powders were fused with Li tetraborate followed by acid digestion, and then analysis using inductively coupled plasma methods (ICP) coupled to atomic

emission spectrometry (ICP-OES) and mass spectrometry (ICP-MS). For F and Cl contents, the samples were fused with KOH and analyses conducted with an ion specific electrode (ISE).

Experimental procedure

The partial melting experiments were done using the piston cylinder apparatus at the Rensselaer Polytechnic Institute (RPI), Troy, NY, USA (Sallet et al, 2015; 2018). The anatexis of two-mica bearing rocks was simulated under three conditions: (i) H_2O-HF fluid present at 725 °C and 0.4 GPa; (ii) fluid absent, designed to simulate muscovite dehydration melting at 700 and 750 °C, and 0.4 and 0.6 GPa, respectively; and (iii) fluid absent, simulating biotite dehydration melting at 930 °C and 0.6 GPa. The capsules loaded with sample powder were kept overnight at 110 °C. For fluid added runs, 4M HF and doubled distilled H_2O were added with a micro syringe after the sample powder immediately before capping and loading the capsule into the piston cylinder press. The duration of the experiments was from 24 to 72 hours (Table 3). The oxygen fugacity during the experiments was unconstrained, but it was presumably below the magnetite-wustite buffer due to the use of a standard graphite heater assembly (e.g., Médard et al., 2008).

Electron probe microanalysis (EPMA)

Major elements, including F, and Cl, in the experimentally derived glass and micas were microanalyzed using a CAMECA SX100 electron probe at RPI (Table 3). Attempts to characterize the Cl content yielded consistently low Cl contents near the detection limit of

the analytical methods used (Sallet et al. 2015, 2019). Analyses applied an accelerating voltage of 15 kV. Calibration and internal standards used EPMA standard minerals (including micas) and glasses (USNM silicates and oxides, RPI F-standard set). Fluorine peaks and backgrounds were combined from counts determined using LPC crystals within two spectrometers. X-ray peaks were counted for 60 s and backgrounds for 30 s. PAP matrix corrections were applied using Cameca software.

The mica compositions were determined using a 100-nA sample current and a spot diameter of 10 μm with F detection limits of 120-160 ppm and precision of ± 3.5 %. For small mica grain size bellow 10 μm we used 20 nA current on a spot size of 2 μm with detection limits of 240 to 320 ppm and precision of ±10%.

For the glass analyses, we applied a defocused fixed spot of 10 μm at two current settings, 5 and 20 nA, to accurately assess the contents of alkalis, aluminum and silicon, which are elements prone to mobility during the EPMA of hydrous glass (Morgan and London, 1996, 2005). We corrected the alkali concentrations by using a linear extrapolation to 0 nA from 20- and 5-nA spot series (Sallet et al., 2015). The F contents were determined with 20 nA beam spots with detection limit of 400 ppm. The analytical precision indicated by one standard deviation varies from 0.04 % to 0.07 % when the F content varies from 0.15 to 2.75 wt%.

The composition of the experimental products was also characterized using scanning electron microscope (SEM), LEO440, coupled with X-ray dispersive energy spectrometer (EDS) with solid state Si(Li) detector and Inca 300 software Oxford Instruments at the Institute of Geosciences, University of São Paulo (USP), São Paulo, Brazil.

RESULTS

Partially melted starting material composition

Backscatter electron (BSE) imaging of muscovite dehydration melting runs at 750 °C and 0.4 GPa, using both the synthetic (MF15) and natural (MF17) two-mica schist (Table, 3), has shown that the biotite is still stable without major textural modification (Figs. 1a,e). Minor micrometric ilmenite ± melt layers along the biotite cleavage is locally observed (Figs. 1c,e). Magnetite rarely coexists with ilmenite in these layers.

The reacted synthetic two-mica rich schist (MF15) revealed large melt pockets around the partially melted quartz and plagioclase grains interconnected with a laminar melt framework interstitially distributed between the neo-formed phases resulting from the incongruent muscovite breakdown (Figs. 1a,b). Such a melt distribution pattern resembles those obtained by the partial melting of millimetric paragneiss cores (Michaud et al. 2021).

Muscovite broke down to form a honeycomb framework of sillimanite needles filled with glass + new biotite + sillimanite ± alkali feldspar ± hercynite (Figs. 1b,c,e). Sillimanite occurs in both acicular and prismatic crystals and forms very fine-grained layers parallel to the capsule wall (Fig. 1e).

Runs with the mica poor starting schist (MLIM) show melting reactions that are similar to the mica-rich layered runs using the MF15 schist. However, melt production is limited to the few muscovite grains and to the nearby surrounding quartz and plagioclase, forming isolated intergranular melting pockets.

Mica composition

EPMA was performed on the starting muscovite and biotite, and on the experimentally derived micas, in runs using natural muscovite and biotite from the two schist samples PPL18 and MLIM, synthetic two-mica schist samples (MF run series), and a synthetic leucocratic glass seeded with biotite. In Table 4 we show the average composition of the large residual biotite after all runs divided by its starting composition (sm/exp ratio) (Fig. 1). The data indicate that F, Cl, and end member compositions (X_{Phl}, X_{Sid}, and X_{Ann}) of the starting biotite remain unchanged after the runs. The PPL18 biotite shows some modification from its starting composition with 15 % less Ti by the end of the runs. All other elements show variations that are lower than 10 %. The MLIM biotite shows variations below 10 % for all the elements. All the EPMA data is available as Supplemental Material 1

The neo-formed biotite grains from the runs are difficult to analyze due to their small size, with typical sections less than 5 μm (Fig.1). Here a 1 μm electron beam spot and a lower current of 5 nA was used, which made the EPMA less accurate for F (Sallet et al. 2018). We show in Table 5 the obtained mean composition of the larger biotite grains, i.e., $0.3 < X_{Phl} < 0.5$; $0.36 < X_{Sid} < 0.62$; and $0.07 < X_{Ann} < 0.17$ (Fig. 2a). These values do not deviate significantly from those of the starting biotite.

The F contents of the starting and neo-formed biotite are expressed in terms of the F intercept value of Munoz (1984), $IV(F) = 1.52X_{Mg}+0.42X_{An}+0.20X_{Sid} - \log (X_F/X_{OH})$, plotted against X_{Mg} in Figure 2b. This parameter allows correction of the F concentration in biotite with respect to the Fe-avoidance effect. Low values of IV(F) correspond to high F contents. The F content of the neo-formed biotite is sensitive to the F content of the starting micas as well as to the addition of HF. Their F content varies widely from 0.44 to 5.08 wt% and the obtained IV(F) varies from 0.46 to 2.06.

Utilizing the run temperature, the fluid parameter $\log(f_{HF}/f_{H2O}) = 2100/T(K) + IV(F)$ (Munoz, 1984) was calculated to range from 2.6 to 4.0 during the crystallization of the neo-formed biotite. This range in fluid composition agrees well with the one obtained for F in biotite from the barren and mineralized granitoids of New Brunswick, Canada (Azadbakht et al. 2020).

Glass composition

EPMA of the glasses obtained from the partial melting of the natural and synthetic two-mica starting materials is given in Table 3 and Figure 3. The multi-cation diagram R2-R1 of de la Roche et al. (1980), and the Modified Alkali-Lime Index (MALI) of Frost et al. (2000), classify the obtained glass as alkali calcic granite to alkalic granite. Its Alumina Saturation Index (ASI) shows a strong peraluminous nature with $1.2 < ASI < 1.8$. The low amounts of the mafic oxides, $M = FeO + TiO_2 + MgO < 4.0$ wt%, and the high $FeO/(FeO + MgO)$ and $K_2O/(K_2O + Na_2O)$ ratios classify the obtained glass as a leucocratic, ferroan, potassic granite melt. All the EPMA data is available as Supplemental Material.

Figure 3 shows the fractionation trends of the major element parameters and F between the partially melted, natural, and synthetic schist samples, and the obtained glasses. The schist residue strongly retained the mafic oxides (Figs. 3b,c,d) while the melt strongly concentrates SiO_2 (Fig. 3a). The alumina saturation index shows a slight decrease in the melt compared to the starting schists (Fig. 3b). The alkalinity shows variable trends with a small decrease for the synthetic MF15 and MF15C schists and for the MLIM schist, and a minor increase for the PPL18 schist (Fig. 3d).

The F content of the starting materials shows a direct correlation trend with the F content of the obtained glasses (Fig. 4). For experiments with added HF, the F content of the starting material was recalculated (Table 1). The fluid-absent runs plot along a linear trend with a high slope and $R^2 = 0.8$. On the other hand, the three HF-assisted runs determine a low slope linear trend. The glasses obtained by muscovite breakdown in the synthetic schists, MF15 and MF15C, show a gentle decrease compared to the starting material (Fig. 3c).

The partial melting of the natural PPL18 and MLIM schists yielded glass with F contents similar to those of the starting material, except for the HF-assisted runs. The F-rich, two-mica schist sample PPL18 yielded a glass with a F content of 0.56 wt% by biotite dehydration melting, 0.43 wt% by muscovite dehydration melting, and 2.77 wt% under HF-assisted partial melting (Table 3).

The F-poor, two-mica schist (MLIM) produced a glass with similar F values between 0.11 and 0.13 F wt% for both H_2O-assisted and mica dehydration partial melting. Under HF-assisted condition, the glass contained 1.12 wt% F.

Added fluid, both HF-bearing or pure H_2O, changed the composition of the glass. HF assisted runs generated F-rich, strongly peraluminous, Na-rich granitic melts by decreasing the alkali-feldspar/plagioclase ratio of the melt. There was also a consistent retention of MgO in the residual solid while Na_2O and CaO dissolved into the melt (Table 3). The pure H_2O run (PM19) produced a strongly peraluminous, high CaO and MgO granitic melt as previously shown for a set of varied starting rock compositions in Sallet et al. (2015).

We calculated the normative composition of the experimental glasses and plotted the results on a Q-Kfs-Ab plot (Table 3; Fig. 5). Multi-cationic parameters (Debon and Le Fort 1988) were used to calculate the quartz content using $Q = Si/3 – (K + Na + 2/3\ Ca)$, and the

feldspar content using F = 555 – (Q + B) where B = Fe + Mg + Ti. The K-feldspar/albite ratios were calculated by assuming that all the K and Na are in these two phases, respectively. The glass Q-Kfs-Ab composition obtained from the muscovite dehydration melting runs show the predominance of potassic feldspar and quartz over albite. In the Q-Kfs-Ab diagram these glasses plot away from the granite eutectic towards the Q-Kfs join.

Natural F partitioning between biotite and muscovite

EPMA of the F content of naturally coexisting biotite and muscovite were conducted in 26 samples from the main Seridó Belt lithologic units (Sallet et al. 2015) (Table 6; Fig. 6). The Seridó schist samples with biotite and muscovite are from regional profiles and from the contact with pegmatitic granites. In both cases muscovite developed later than the metamorphic biotite. In samples from the Jucurutu gneiss, which is a meta-greywacke (Sallet et al. 2015, 2021), muscovite occurs as tiny crystals within the rock matrix. The samples from the Acari granite pluton are from a meter wide muscovitized shear zone at the contact with the Seridó mica schist (Sallet et al. 2018). Lastly, we sampled micas from pegmatitic granites where biotite coexists with muscovite.

All the data plot along a straight line in the diagram F Bt % vs F Ms % yielding an average $Kd(F)^{Bt/Ms} = F(Bt) / F(Ms) = 2.7 \pm 0.5$ (Table 6, Fig. 6a). The data was also plotted using the intercept value IV(F) (Munoz 1984; Munoz and Ludington 1977). Here F enrichment in muscovite and biotite correspond to a decrease in IV(F) (Fig. 6b). Despite the variety of processes behind the formation of the micas and the wide range in F from muscovite and biotite, the data plot with a high correlation coefficient, R^2.

Compared to earlier determinations, the $Kd(F)^{Bt/Ms}$ obtained in this study is greater than those obtained for two-mica granites in Portugal, where $Kd(F)^{Bt/Ms} = 1.8$ (Neiva et al. 2002; Neves 1997). They are statistically similar to those in the Himalayas of southern Tibet where $Kd(F)^{Bt/Ms} = 2.2$ (Xie et al. 2020). On the other hand, metamorphic rocks from western Labrador, Canada, yielded a greater $Kd(F)^{Bt/Ms}$ value of 3.7 (Yang and Rivers 2000).

DISCUSSION

Muscovite dehydration melting reaction

We estimated the normative composition of the MF run series capsules by mass balance calculations using the starting material, glass, and mica compositions along with BSE image analysis (Table 7). The capsule images indicate that nearly all the muscovite broke down while the initial biotite remained stable.

Imparting appropriate constraints derived from the starting material composition and image analysis, we utilized an iterative routine in Microsoft Excel to determine the normative composition of the capsule (Supplemental Material 2). We applied a convergence factor of ± 10 wt% for each chemical element between the starting material and the obtained mass balance composition. We also imposed mininal values to the error sum of the squares leading to an average convergence of 1.0 ± 0.1.

Assuming that the biotite remained stable during the experimental runs, we fixed the starting biotite proportion at 51 wt%. According to the image analyses we used an upper limit value for muscovite and alkali feldspar of ≤ 4 wt% and a minimum content of ~~6 and~~ 7 wt% for quartz. The obtained partial melting rate is between 15 to 18 wt% for runs with both F-

poor PReg muscovite and F-rich ASM muscovite. The obtained average composition of the five runs, starting with the synthetic two-mica schist (Table 7), allows us to determine the stoichiometric coefficients for the muscovite dehydration melting reaction as:

muscovite + 0.25 quartz = 0.53 melt + 0.25 sillimanite + 0.22 biotite + 0.13 K-feldspar (1)

Small amounts of hercynite and ilmenite, and traces amounts of magnetite make less than 1.0 wt% of the normative composition (Figs. 1 c,d). As biotite is stable after the runs, the Fe and Ti contents incorporated to neoformed phases should come only from the starting muscovite, with FeO and TiO_2 average contents of 1.9 and 0.6 wt %, respectively (Supplemental Material). The biotite chemical stability is evidenced by the absence of substantial variations in biotite end member compositions (X_{Phl}, X_{Sid}, and X_{Ann}) after the runs, and by glasses that are more leucocratic (low M) than the starting muscovite (Tables 2 and 3).

Fluorine partitioning between biotite and peraluminous melt

We assessed the partition coefficient between the neo-formed biotite and coexisting melt, i.e., $Kd_{(F)} = (F)_{biot} / (F)_{melt}$, for a series of seven experiments (Table 8; Fig. 7). The obtained $Kd_{(F)}$ value varies between 1.9 and 5.6 with an average $Kd_{(F)} = 3.0 \pm 1.3$. It is noteworthy that for our three HF-assisted runs we obtained low $Kd_{(F)}$ values and neo-formed biotite with a low MgO content. Also, the high-temperature dry run with the F-rich starting schist PPL18 yielded a higher $Kd_{(F)}$ and a higher MgO content in the biotite than the run with the F-poor schist MLIM.

Comparing our results with earlier experimental studies, Icenhower and London (1997) obtained a similar $Kd_{(F)}$ range of 1.6 to 7.2 for the peraluminous melts, with an average of 4.0 ± 2.0. Fluorine partitioning between biotite and the meta-aluminous melts, as described by Zhang et al. (2022), yielded a $Kd_{(F)}$ with an average value of 3.4 ± 1.1. In contrast, the dehydration melting of a two-mica metapelite by Pickering and Johnston (1998) yielded a significantly higher $Kd_{(F)}$ between 4 and 12.

It is well known from experimental and natural data that both MgO and F in biotite increase with increasing temperature (e.g., Patiño Douce and Harris 1998; Peterson et al. 1991; Sallet et al. 2015). Such a relationship has been shown for the partial melting of peraluminous protoliths but not for metaluminous protoliths (Fig. 7). In the case of peraluminous melts we fitted $Kd_{(F)}$ vs. MgO (biotite) using our data along with the results from Icenhower and London (1997) to obtain:

$$Kd_{(F)} = 0.39\ (MgO)_{biot} - 0.65, \quad R^2 = 0.87 \tag{2}$$

The correlation between $Kd_{(F)}$ vs. MgO (biotite) obtained using the data from Pickering and Johnston (1998) shows a significantly steeper slope (Fig. 7). With respect to the experimental conditions, this difference is probably due to the higher pressure of 1.0 GPa used by Pickering and Johnston (1998) as compared to 0.4 and 0.6 GPa used in in this study, and the 0.2 GPa used by Icenhower and London (1997).

Fluorine partitioning model between an anatectic melt, micaceous restite, and fluid

The obtained F partition coefficients from this study, along with data from earlier experimental studies, have allowed us to model the distribution of F between melt, residual

This is the peer-reviewed, final accepted version for American Mineralogist, published by the Mineralogical Society of America.
The published version is subject to change. Cite as Authors (Year) Title. American Mineralogist, in press.
DOI: https://doi.org/10.2138/am-2022-8663. http://www.minsocam.org/

micas, and associated fluids (Icenhower and London 1997; Patiño Douce and Harris 1998; Pickering and Johnston 1998; Webster and Holloway, 1990).

We used the obtained relationship $Kd_{(F)} = 0.39\ (MgO)\ (Bt) - 0.65$ to calculate $Kd_{(F)}$ and F in the melt and the micas as a function of the MgO and F contents in the biotite. In Table 8 we show that the obtained mean $Kd_{(F)}$ obtained from these studies ranges from 3.3 ± 0.9 to 4.0 ± 2.1 with a total mean $Kd_{(F)} = 3.6 \pm 1.2$ for 48 samples. We standardized the available experimental data obtained for $Kd_{(F)}$ using our fitted $Kd_{(F)} = 0.39\ (MgO)(Bt) - 0.65$, which decreased the calculated $Kd_{(F)}$ from 8.2 ± 2.4 to 3.6 ± 0.8 (Fig. 7).

To assess the F composition of a fluid phase coexisting with the melt and micaceous residue, we fitted the experimentally determined F partition coefficients between the fluid and peraluminous melt obtained by Webster and Holloway (1990). The F enters the fluid in greater amounts under a high F content according to the relationship: $D_F = 0.09\ (F) + 0.24$, $R^2 = 0.85$.

We calculated a F bulk partition coefficient residue/melt, $D_{F_{melt}}^{res}$, using the obtained melting rates X_{melt} along with the F contents of the starting materials and glass (Table 8), and with data from previous results obtained by Sallet et al. (2019):

$$D_{melt}^{res} = \frac{1}{(F)_{melt}}\left[\frac{(F)_{sm} - X_{melt}\,(F)_{melt}}{1 - X_{melt}}\right] \quad (3)$$

$$(F)_{sm} = starting\ material\ concentration$$

In this study the experiments were done using F-rich protoliths as compared to our previous runs, which used F-poor protoliths as represented by the regional Seridó mica schist belt (Sallet et al. 2015, 2019). The obtained data set, plotted in Figure 8, shows the control exerted by the starting F content of the melted protolith on $D_{F_{melt}}^{res}$. The F bulk partition

coefficient varies following both linear and logarithmic increases from 0.5 to 3.5 as the protolith F content evolves from near zero to 1.5 wt%. This $D_{F_{melt}}^{res}$ range is significantly higher than the one of 0.2 to 0.9 reported for $D_{F_{melt}}^{fluid}$ by Webster and Holloway (1990). It agrees with the contrasted slopes shown in Figure 4 indicating that F enter more effectively the melt from the fluid than from the mica dehydration melting.

In Figure 9a we show the theoretical framework for the distribution of F between the melt and residual biotite considering the case where $Kd_{(F)}$ varies with the MgO content of the biotite. We also plot in Figure 9a all the available standardized $Kd_{(F)}$ data (Icenhower and London 1997; Patiño Douce and Harris 1998; Pickering and Johnston 1998). We see that results obtained using a muscovite + biotite protolith, with no added HF, corresponds to a F-poor, melt-mica-fluid system, whereas using dry F-rich starting materials with added H_2O and/or HF led to F-rich systems. Consequently, the F content of an anatectic peraluminous melt depends on the F and MgO contents of the muscovite and biotite from the melted rock.

Two-mica protoliths with a high Fe/(Fe+Mg) and F-rich micas will generate a progressively F-enriched leucosome, neo-formed biotite, and fluid, if present, with increasing F in the residual biotite. Such a model agrees with previous study data that shows a negative correlation between IV(F) and X_{Mg} in metamorphic biotite obtained from across the de Seridó biotite schist belt (Sallet et al. 2019). Similar enrichment in F is present in the Fe- and F-rich Tabuleiro granites compared to the F-poor and Mg-rich Pedras Grandes granite in the NE extremity of the Neoproterozoic Pelotas Batholith, southern Brazil (Sallet et al. 1997, 2000).

In the case in which a fluid phase coexists with a peraluminous melt we calculated the F content using the data obtained by Webster and Holloway (1990) and the relation $D_F = 0.09$ (F) + 0.24. It applies to both external fluid flux during anatectic processes and fluid exsolved

from peraluminous melts. The F contents of the fluid depends on the F contents of the coexisting micas and their Fe/(Fe+Mg) (Fig. 9b). The partial melting of an Fe- and F-rich schist results in the F-richest peraluminous melts. For example, a fluid phase with 1 wt% of F will coexist with an Mg-poor biotite, (MgO = 2.5 wt%), with a F content of 0.75 wt%. On the other hand, a fluid with 1 wt% F concentration will coexist with a Mg-richer biotite (MgO = 10 wt%) and a F content of 7.5 wt%.

This behavior seen for F suggests that Fe-rich protoliths and melts are potentially associated with F-rich fluids during both crustal anatexis and melt crystallization. The F-rich and strongly peraluminous Macusani glass falls within the F compositional range obtained from the HF-assisted runs. Its biotite composition falls within the interval $2.6 < \log(f_{H2O}/f_{HF}) < 3.2$ at 700 to 725 °C. Such $\log(f_{H2O}/f_{HF})$ compositions are like those obtained for F-rich granitic biotite from the Sn-W mineralized systems of the New Brunswick pluton, Canada (Azadbakht et al. 2020). Enrichment in Li, Be, Cs, Nb, Ta, W, Sn, and U is commonly associated with F-rich peraluminous leucogranitic melts and related fluids (e.g., Cuney et al. 2002; Harlaux et al. 2017; Linnen et al. 2012). Therefore, metal enrichment of peraluminous leucogranitic liquids generated by muscovite dehydration melting must consider F and metal-rich, muscovite-rich protoliths.

IMPLICATIONS

The experiments from this study have resulted in strongly peraluminous melts coexisting with a peraluminous residual mineral assemblage. The muscovite dehydration melting experiments, starting with two-mica protoliths, have shown a layered melt distribution where the muscovite-rich layers give rise to melting reactions while the biotite layers remained

inert. Such a melt distribution pattern reproduces the common layered migmatite, which can serve as melt pathways during crustal anatexis. The partial melting of a non-layered, muscovite-poor schist resulted in unconnected melt pockets.

The experimentally observed resulting residual mineral association is typically composed of biotite(1) ± quartz ± plagioclase ± muscovite and neo-formed melt + biotite(2) + sillimanite + alkali feldspar ± Fe-Ti oxides ± hercynite. Such mineralogical features, particularly the textural and chemical distinctions between the two generations of biotite, could be a useful tool for petrogenetic studies of peraluminous migmatites. These are prograde dehydration reactions and textures that may not be preserved in natural examples due to retrograde overprinting.

The melt fraction obtained by muscovite dehydration depends on the relative proportions between the micas (muscovite and biotite), quartz, and feldspar. The data from this study, along with the results from Sallet et al. (2015), have shown that experimental mica dehydration yields low melting rates below 30 wt% while H_2O-added runs yielded melt rates of up to 50 wt%. The obtained results suggest that the muscovite dehydration melting rate would not be enough to allow for melt migration ~~and coalescence into large plutons, but instead would~~ forming dikes and sills typical of a near *in situ* peraluminous metatexite. On the other hand, under the external influx of H_2O, the melt production should be sufficient for melt migration and the generation of peraluminous diatexites, granites, and pegmatites.

Our experimental determination of F partitioning coefficients, with those data obtained in earlier studies, produce a framework showing the F partitioning data between melt, muscovite, biotite, and fluid during the anatexis of two-mica-rich protoliths.. The obtained results indicate that the F content of the generated leucosome is proportional, not only to the

F content of the mica in the protolith, but also to the FeO/(FeO + MgO) ratio in the biotite. Ferroan peraluminous schists and granites, will generate F-rich peraluminous melts; in contrast, the anatexis of a Mg-rich schist will generate F-poor melts. The mean value for $Kd_{(F)} = (F)_{Bt}/(F)_{melt}$ in the model allows us to link the F content of peraluminous granites and pegmatites to the F content of the neo-formed mica in the anatectic residue and *vice versa*.

The available MgO and F contents from the stabilized biotite in the partial melting experiments of the natural, two-mica schist yield F melt concentrations varying from a few hundreds to a few thousand ppm, which is the range typically found in peraluminous granites and pegmatites (e.g., Sallet, 2000). As F does not show an affinity for the aqueous fluid phase, the modeled fluid F contents are low and vary from tens to thousands of ppm, depending on the MgO and F content of the biotite.

Finally, our data suggest that the detailed F systematics in muscovite and biotite from the paleosome, melanosome, and leucosome of peraluminous migmatites can be a useful tool in the study of their petrogenesis. The estimation of the F content of the fluid, related to the anatexis of peraluminous rocks, could also be useful in research on the origin of rare metal and U mineralization associated with peraluminous granites and pegmatites.

ACKNOWLEDGEMENTS

RS and JP thanks Bruce Watson for encouragements, insights, and use of the experimental and analytical facilities at Rensselaer Polytechnic Institute, Troy, NY, USA.; David Wark for EPMA calibration, RS thanks Robert Moritz for analytical facilities at the University of Geneva, Switzerland. National Science Foundation EAR-0635858 is acknowledged for

support of some of the experiments in this study. MHH is grateful to the CNPq for the research fellowship 303201/2019-3. We appreciated the careful reviews from an anonymous reviewer and D. Foustoukos.

REFERENCES CITED

Acosta-Vigil, A., London, D., and Morgan, G.B. VI (2006) Experiments on the kinetics of partial melting of a leucogranite at 200 MPa H_2O and 690-800°C: compositional variability of melts during the onset of H_2O-saturated crustal anatexis. Contributions to Mineralogy and Petrology, 151, 539-557.

Anenburg, M., and Katzir Y. (2014) Muscovite dehydration melting in Si-rich metapelites: microstructural evidence from trondhjemitic migmates, Rodes, Israel. Mineralogy and Petrology, 108, 137-152.

Azadbakht, Z., Lentz, D.R., McFarlane, C.R., and Whalen, J.B. (2020) Using magmatic biotite chemistry to differentiate barren and mineralized Silurian–Devonian granitoids of New Brunswick, Canada. Contributions to Mineralogy and Petrology, 175, 69.

Beard, J.S. and Lofgren, G.E. (1991) Dehydration-melting and water-saturated melting of basaltic and andesitic greenstones and amphibolites at 1, 3, and 6.9 Kb. Journal of Petrology, 32, 365-401.

Beard, J.S., Lofgren, G.E., Sinha A.K., and Tollo R.P. (1994) Partial melting of apatite-bearing charnockite, granulite, and diorite: Melt compositions, restite mineralogy, and petrologic implications. Journal of Geophysical Research, 99, 21591-21603.

Brearley, A.J. and Rubie, D.C. (1990) Effects of H_2O on the disequilibrium breakdown of muscovite + quartz. Journal of Petrology, 31, 925 – 956.

Carroll, M. and Wyllie, P. (1990) The system tonalite-H_2O at 15 kbar and the genesis of calc-alkaline magmas. American Mineralogist, 75, 345-357.

Castro, A., Corretgé, L.G., El-Biad, M., El-Hmidi, H., Fernández, C., and Patiño Douce, A.E. (2000) Experimental constrains on the Hercinyan anatexis in the Iberian Massif, Spain. Journal of Petrology, 41, 1471-1488.

Cuney, M., Alexandrov, P., Le Carlier de Veslud, C., Cheilletz, A., Raimbault,L., Ruffet, G., and Scaillet, S. (2002) The timing of W–Sn-rare metals mineral deposit formation in the Western Variscan chain in their orogenic setting: the case of the Limousin area (Massif Central, France). Geological Society, London, Special Publications, 204, 213-228.

De la Roche, H.D., Leterrier, J.T., Grandclaude, P., and Marchal, M. (1980) A classification of volcanic and plutonic rocks using R1R2-diagram and major-element analyses—its relationships with current nomenclature. Chemical Geology, 29, 183-210.

Debon, F. and Le Fort, P. (1988). A cationic classification of common plutonic rocks and their magmatic associations: principles, method, applications. Bulletin de Minéralogie, 111, 493-510.

Dyck, B., Waters, D.J., St-Onge, M., and Searle, M. (2019) Muscovite dehydration melting: Reaction mechanisms, microstructures, and implication for anatexis. Journal of Metamorphic Geology, 38, 29-52.

Fink E.G. and Thomkins, A.G. (2017) Fluorine and chlorine behaviour during progressive dehydration melting: Consequences for granite geochemistry and metallogeny. Journal of Metamorphic Geology, 35, 739-757.

Frost, B.R., Barnes, C.G., Collins, W.J., Arculus, R.J., Ellis, D.J., and Frost, C.D. (2001) A geochemical classification for granitic rocks. Journal of Petrology, 42, 2033-2048.

Gao, P., Zheng, Y., and Zhao, Z. (2016) Experimental melts from crustal rocks: A lithochemical constraint on granite petrogenesis. Lithos, 266-267, 133-157

Gardien, V., Thompson, A.B., Grujic, D., and Ulmer, P. (1995) Experimental melting of biotite + plagioclase + quartz ± muscovite assemblages and implications to crustal melting. Journal of Geophysical Research, 100, 15581-15591.

Gardien, V., Thompson, A.B., and Ulmer P. (2000) Melting of biotite + plagioclase + quartz gneisses: the role of H_2O in the stability of amphibole. Journal of Petrology, 41, 651-666.

Genier, F., Bussy, F., Epard, J.L., and Baumgartner, L. (2008) Water-assisted migmatization of metagraywackes in a Variscan shear zone, Aiguilles–Rouges massif, western Alps. Lithos, 102, 575–597.

Harlaux, M., Mercadier, J., Bonzi, W.M, Kremer, V., Marignac, C., and Cuney M. (2017) Geochemical signature of magmato-hydrothermal fluids exsolved from the Beauvoir rare-metal granite (Massif Central, France), Insights from LA-ICPMS analyses of

primary fluid inclusions. In Ding, X., Harlov, D.E., Chen, B., Sun, W. Fluids, Metals and Mineral/Ore Deposits, p. 123-156. Geofluids, Special Issue.

Hansen E.C. and Harlov D.E. (2007) Whole rock, phosphate and silicate compositional trends across the amphibolite-to granulite-facies transition, Tamil Nadu, India. Journal of Petrology, 48, 1641-1690.

Holtz, F. and Johannes, W. (1991) Genesis of peraluminous granites I. Experimental investigation of melt composition at 3 and 5 kb and various H_2O activities. Journal of Petrology, 32, 935-958.

Icenhower, J.P. and London, D. (1997) Partitioning of fluorine and chlorine between biotite and granitic melt: experimental calibration at 200 MPa H_2O. Contributions to Mineralogy and Petrology, 127, 17-29.

Linnen, R.L., Van der Lichtervelde, M., and Cerny, P. (2012) Granitic pegmatites as sources of strategic metals. Elements, 8, 275-280.

Luth, W.C., Jahns R.H, and Tuttle, O.F. (1964) The granite system at pressures of 4 to 10 Kb. Journal of Geophysical Research, 69, 759-773.

Médard, E., McCammon, C.A., Barr, J.A., and Grove, T.L. (2008) Oxygen fugacity, temperature reproducibility, and H_2O contents of nominally anhydrous piston-cylinder experiments using graphite capsules. American Mineralogist, 93, 1838–1844.

Michaud, J. A.S, Pichavant, M., and Villaros, A. (2021) Rare elements enrichment in crustal peraluminous magmas: insights from partial melting experiments. Contributions to Mineralogy and Petrology, 176, 96.

Morgan, G.B., VI and London, D. (1996). Optimizing the electron microprobe analyses of hydrous alkali aluminosilicate glasses. American Mineralogist, 81, 1176-1185.

Morgan, G.B. VI and London, D. (2005). Effect of current density on the electron microprobe analyses of alkali aluminosilicate glasses. American Mineralogist, 90, 1131-1138.

Munoz, J.L. (1984) F-OH and Cl-OH exchange in micas with application to hydrothermal ore deposits. Mineralogical Society of America, Reviews in Mineralogy, 13, 469-493.

Munoz, J.L. and Ludington, S. (1977) Fluorine-hydroxyl exchange in synthetic muscovite and its application to muscovite-biotite assemblages. American Mineralogist, 62, 304-308.

Nabelek, P.I. (2020) Petrogenesis of leucogranites in collisional orogens. Geological Society, London, Special Publications, 491, 179-207.

Neiva, A.M.R., Silva, M.M.V.G, Gomes, M.E.P, and Campos, T.F.C. (2002) Geochemistry of coexisting biotite and muscovite of Portuguese peraluminous granitic differentiation series. Chemie der Erde, 62, 197-215.

Neves, L.J.P.F. (1997) Trace element content and partitioning between biotite and muscovite of granitic rocks: a study in the Viseu region (Central Portugal). European Journal of Mineralogy, 9, 849-858.

Patiño Douce, A.E. and Beard, J.S. (1995) Dehydration-melting of biotite gneiss and quartz amphibolites from 3 to 15 kbar. Journal of Petrology, 36, 707-738.

Patiño Douce, A.E. and Harris, N. (1998) Experimental constrains on Himalayan anatexis. Journal of Petrology, 39, 689-710.

Peterson, J.W., Chacko, T., and Kuehner, S.M. (1991) The effects of fluorine on the vapor-absent melting of phlogopite + quartz: implications for deep-crustal processes. American Mineralogist, 76, 470-476.

Pickering, J.M. and Johnston, A.D. (1998) Fluid-absent melting behavior of a two-mica metapelite: experimental constraints on the origin of Black Hills granite. Journal of Petrology, 39, 1787-1804.

Sallet, R. (2000) Fluorine as a tool in the petrogenesis of quartz-bearing magmatic associations: applications of an improved F-OH biotite-apatite thermometer grid. Lithos, 50, 241-253.

Sallet, R., Moritz, R., and Fontignie, D. (2000) Fluorite $^{87}Sr/^{86}Sr$ and REE constraints on fluid–melt relations, crystallization time span and bulk D_{Sr} of evolved high-silica granites. Tabuleiro granites, Santa Catarina, Brazil. Chemical Geology, 164, 81-92.

Sallet, R., Price, J.D., and Moritz, R. (2018) Natural and experimental fluorine substitution in biotite: Implications for fluid-rock thermochronometry and application to the Seridó Belt, northeastern Brazil. Chemical Geology, 482, 32-45.

Sallet, R., Moritz, R., and Sabatier, H. (1997) Geochemistry of the Tabuleiro fluorite high silica granites: Pelotas Batholith, southern Brazil - Potential for Sn-Mo mineralizations. In Papunen, H., Eds., Conference: Mineral Deposits: Research and Exploration Where do They Meet?, p. 667-670. Turku, Finland.

Sallet, R., Vital, H., Price, J.D., and Moritz, R. (2019) The geochemical behavior of F and Cl during the weathering–diagenesis–metamorphism–anatexis cycle. Insights from the clay fraction of fine sands from the Amazon River mouth and metapelititic rocks from the Seridó Belt, Brazil. Chemical Geology, 525, 260-267.

Sallet, R., Price, J.D., Babinski, M., Moritz, R., Souza, Z.S., and Chiaradia, M. (2015) Experimental anatexis, F geochemistry and lead-isotope constraints on granite petrogenesis in the Seridó Belt, Boroborema Province, Northeastern Brazil. Chemical Geology, 400, 122-148.

Sallet, R., Ribeiro, C., Souza Neto A., Sales, M., Moritz, R., Price, J.D., and Thomsen, T.B. (2021) Pegmatitic granite fluid compositions and thermochronometry in the Seridó Belt, Borborema Province, Brazil: Insights from trace element advection-diffusion-partitioning halos in host schist and gneiss. Lithos, 396-397, 106200.

Sawyer, E.W. (2010) Migmatites formed by water-fluxed partial melting of a leucogranodiorite protolith: Microstructures in the residual rocks and source of the fluid. Lithos, 116, 273-286.

Skjerlie, K.P. and Johnston, A.D. (1993) Fluid-absent melting behavior of an F-rich tonalitic gneiss at mid-crustal pressures: Implications for the generation of anorogenic granites. Journal of Petrology, 34, 785-815.

Skjerlie, K.P. and Johnston, A.D. (1996) Vapour-absent melting from 10 to 20 kbar of crustal rocks that contain multiple hydrous phases: implications for anatexis in the deep to very deep continental crust and active continental margins. Journal of Petrology, 37, 661-691.

Storre, B. (1982) Dry melting of muscovite + quartz in the range P_S = 7 GPa to P_S = 20 GPa. Contributions to Mineralogy and Petrology, 37, 87 - 89.

Thompson, A.B. (1982) Dehydration-melting of metapelites and the generation of H_2O undersaturated granitic liquids. American Journal of Science, 282, 1567-1595.

Vielzeuf, D. and Holloway, J.R. (1988) Experimental determination of the fluid-absent melting relations in the pelitic system. Consequences for crustal differentiation. Contributions to Mineralogy and Petrology, 98, 257-276.

Webster, J. D. and Holloway, J. R. (1990) Partitioning of F and Cl between magmatic hydrothermal fluids and highly evolved granitic magmas. In Stein, H.J. and Hannah, J.L., Eds., Ore-bearing Granite Systems: Petrogenesis and mineralizing processes, 246, p. 21-34. GSA Special Papers.

Weinberg, R.F. and Hasalovà P. (2015) Water-fluxed melt of the continental crust. A review. Lithos, 212-215, 158-188.

Wise M.A., Muller A., Simmons W.B. (2022) A proposed new mineralogical classification system for granitic pegmatites. Canadian Mineralogist, 60, 229-248.

Xie L., Tao, X., Wang, R., Wu, F., Liu, C., Liu, X., Li, X., and Zhang, R. (2020) Highly fractionated leucogranites in the eastern Himalayan Cuonadong dome and related magmatic Be-Nb-Ta and hydrothermal Be-W-Sn mineralization. Lithos, 354-355, 105286.

Yang, P. and Rivers T. (2000) Trace element partitioning between coexisting biotite and muscovite from metamorphic rocks, Western Labrador: Structural, compositional and thermal controls. Geochimica and Cosmochimica Acta, 64, 1451-1472.

Zhang, C., Li, X., Behrens, H., and Holtz, F. (2022) Partitioning of OH-F-Cl between biotite and silicate melt: Experiments and an empirical model. Geochimica et Cosmochimica Acta, 317, 155-179.

FIGURE 1. Backscattered electron images (BSE) of the main textural features obtained by muscovite dehydration melting. **a**) Whole capsule view of the MF15C run with synthetic starting two-mica schist. Note the preservation of the starting biotite, the incongruent melting of muscovite leading to melt + sillimanite (Sil) +neo-formed biotite (Bt2) as well as partial melting of quartz (Qz); **b**) High contrast image of Fig. 1a highlighting the connection of reaction sites forming a melt network; **c**) Detail of the neo-formed phases in MF15C: melt, K-feldspar (Kfs), biotite (Bt2), sillimanite (Sil), ilmenite (Ilm); **d**) and **e**) - View of the incongruent melting of muscovite (Ms) in MF17 capsule with natural MLIM two-mica schist as the starting material. Note in **d** the residual muscovite (Ms) associated with melt, and the neo-formed biotite (Bt2), sillimanite (Sil), and hercynite (Hc). **e**. Stable starting biotite (Bt1), the incongruent melting of muscovite (Ms) associated with neo-formed K-feldspar (Kfs), biotite (Bt2), and sillimanite (Sil) and the partial melting of plagioclase (Pl) and quartz (Qz).

FIGURE 2. Major element and F composition of starting and experimental neoformed biotite. **a**) Ternary phlogopite-siderite -annite diagram. **b**) IV(F) vs XMg plot showing the effects of T and HF. IV(F) is the F intercept value (Munoz, 1984).

FIGURE 3. Composition of the starting materials and of the glass obtained by partial melting experiments. **a**) Multi cation R1 vs R2 diagram (de La Roche, 1980). **b**), **c**), and **d**) Alumina Saturation Index (ASI), F, and Modified Alkalinity Index (MALI) (Frost, 2001), respectively, vs. mafic oxides (M) in wt. %. Tie lines link the experimental starting materials to the obtained glasses.

FIGURE 4. The F content in the experimental glass vs. the starting materials.

FIGURE 5. Quartz-albite-K-feldspar ternary plot showing the obtained normative composition of the experimental glass. The cotectic lines and eutectic point are from Luth et al. (1964).

FIGURE 6. a) F distribution between biotite and muscovite from the Seridó mica schist, Jucurutu paragneiss, sheared Acari granite, and Serra Verde pegmatitic granite. **b**) The IV(F) values distribution between biotite and muscovite. The F intercept value for IV(F) is taken from Munoz (1984).

FIGURE 7. Kd(F) = (F)Bt / (F)melt vs. (MgO)Bt diagram. **a**) The obtained Kd(F) in this study compared to previously determined Kd(F). The Kd(F) from this study agrees with Kd(F) values obtained by Icenhower and London (1997). The two data sets combined yield a straight-line Kd(F) = 0.39 (MgO)Bt – 0.65, $R^2 = 0.87$. We also show the Kd(F) obtained by Zhang et al. (2022) for meta-aluminous calc alkalic mafic to felsic melts. **b**) Detailed distribution of the runs from this study along the fitted straight line. It is noteworthy that the runs with added HF yielded a low Kd(F).

FIGURE 8. Experimental determination of the F bulk partition coefficient D_F between the partial melt residue and the melt with F in the protolith. The high values obtained in this study, $2.0 < D_F < 3.5$, are linearly fitted and come from runs with low melting rate of 15 wt%.

The low values, $D_F < 1$, were obtained from runs with high average melting rate of 41 ± 17 wt% (Sallet et al. 2015, 2019). The whole data are logarithmic fitted with high $R^2 = 0.97$.

FIGURE 9. a) Modeled F contents of peraluminous granitic melts coexisting with biotite, neo-formed or re-equilibrated, as a function of its F and MgO contents. The model uses the F partition coefficient as Kd(F) = 0.39 (MgO)Bt – 0.65. **b**) Modeled F contents of a fluid coexisting with melt and micas, neo-formed or re-equilibrated, as a function of their F and MgO contents. The model uses the F partition coefficients given by Kd(F) = 0.39 (MgO)Bt – 0.65 and DF = 0.09 (F) + 0.24. The F content of the residual muscovite is obtained by applying Kd (F)Bt/Ms = 2.7.

This is the peer-reviewed, final accepted version for American Mineralogist, published by the Mineralogical Society of America.
The published version is subject to change. Cite as Authors (Year) Title. American Mineralogist, in press.
DOI: https://doi.org/10.2138/am-2022-8663. http://www.minsocam.org/

TABLE 1. Experiment starting material compositions of natural and synthetic two-mica protoliths. Mineral composition in wt. %. Rock composition obtained by normative calculation. Synthetic schist starting micas labeled as Mus/Bt. F, Cl, and geochemical parameters as ASI = molar Al_2O_3 / ($CaO + Na_2O + K_2O$), MALI = ($K_2O + Na_2O$) - CaO, #K = K_2O / ($K_2O + Na_2O$), ALK = K_2O + Na_2O, mafic oxides M = FeO + MgO + TiO_2, and # Fe = FeO / (MgO + FeO). In parenthesis the starting F contents of runs with added 10 wt% HF 4M.

Sample	SM	Mus	Bt	Pl	Qtz	Mus/Bt	F	Cl	ASI	MALI	ALK	#K	M	#Fe
MLIM	rock	5	23	19	53		0.10 (1.21)		2.50	4.77	5.65	0.77	15.22	0.67
PPL18	rock	29	30	28	13		0.78 (1.61)	0.08	2.81	5.17	5.83	0.77	10.83	0.66
MF15C1	synt. schist	34	51	0	15	Preg/STAN	0.34	0.08	2.30	8.29	8.30	1.00	17.14	0.72
MF15C2	synt. schist	34	51	0	15	Preg/PBT1	0.89	0.02	2.13	8.10	8.10	1.00	17.93	0.66
MF15C3	synt. schist	34	51	0	15	Preg/PPL18	1.21	0.01	2.39	7.83	7.83	1.00	16.86	0.64
MF15a	synt. schist	34	51	0	15	ASM/PBT1	1.18	0.02	2.15	7.95	7.95	1.00	17.93	0.66
MF15b	synt. schist	34	51	0	15	ASM/STAN	0.63	0.08	2.32	8.14	8.15	1.00	17.14	0.72
MF6a	mica mix					PPL18/PPL18	1.40	0.01	2.44	7.56	7.56	1.00	17.01	0.63
MF6b	mica mix					PPL18/StAnd	0.42	0.00	2.62	7.46	7.46	1.00	16.99	0.65
FG8	glass SV0		2.5				0.10 (1.21)	0.00	1.26	7.31	7.49	0.44	1.13	0.73

TABLE 2. Experiment starting mica composition obtained by EPMA. Biotite and muscovite molar end members and IV(F) calculated according to Munoz (1984).

sample	biotite	F	Cl	XMg	Xsid	Xan	IV(F)	ASI	M
MLIM	mean	0.30	0.05	0.69	0.24	0.06	2.56	2.43	30.97
n = 21	σ	0.08	0.01						
PPL18	mean	2.28	0.01	0.72	0.19	0.08	1.6	2.25	30.20
n = 82	σ	0.19	0.01						
STAN	mean	0.53	0.14	0.77	0.18	0.05	2.39	2.06	31.17
n = 11	σ	0.02	0.02						
PBT1	mean	1.61	0.03	0.79	0.1	0.11	1.89	1.68	31.70
n = 15	σ	0.06	0.01						
StAnd	mean	0.3	0.01	0.68	0.27	0.05	2.54	2.56	30.82
n = 101	σ	0.01	0.01						

sample	muscovite	F	Cl	Xal	XFe	XMg	IV(F)	ASI	M
MLIM	mean	0.12	0.00	0.88	0.09	0.03	1.87	3.80	3.79
n = 15	σ	0.02	0.01						
PPL18	mean	0.76	0.01	0.88	0.06	0.06	1.08	3.72	3.43
n = 16	σ	0.06	0.03						
ASM	mean	1.04	0.01	0.89	0.07	0.04	0.9	3.62	2.98
n = 20	σ	0.03	0.01						
Preg	mean	0.20	0.02	0.9	0.07	0.03	1.64	3.53	3.03
n = 12	σ	0.01	0.04						

This is the peer-reviewed, final accepted version for American Mineralogist, published by the Mineralogical Society of America.
The published version is subject to change. Cite as Authors (Year) Title. American Mineralogist, in press.
DOI: https://doi.org/10.2138/am-2022-8663. http://www.minsocam.org/

TABLE 3. Experimental anatexis conditions of natural and synthetic schist and glass compositions obtained by EMPA. Fluorine and Cl in wt%. Geochemical parameters as in Table 1. The normative composition of glass in wt% is given with Kfs – alkali feldspar, Pl – plagioclase, and Qtz – quartz.

Run	SM	T(°C)	P(GPa)	fluid	hours		F	Cl	ASI	MALI	ALK	#K	M	#Fe	Kfs	Pl	Qtz
PM20	PPL18	930	0.6	dry	24	mean	0.55	0.01	1.54	5.94	6.68	0.77	4.05	0.72	0.37	0.16	0.47
						σ	0.03	0.01									
						n	22	22									
PM23	PPL18	775	0.6	dry	24	mean	0.44	0.01	1.57	6.79	7.41	0.80	2.14	0.85	0.43	0.16	0.40
						σ	0.08	0.01									
						n	32	13									
PM22	PPL18	725	0.4	10 % HF 4M	24	mean	2.72	0.01	1.39	6.20	7.42	0.67	1.46	0.89	0.37	0.28	0.34
						σ	0.11	0.01									
						n	21	21									
MF17B	MLIM	930	0.6	dry	24	mean	0.13	0.01	1.18	8.28	9.07	0.73	2.75	0.79	0.43	0.25	0.32
						σ	0.02	0.01									
						n	40	40									
MF17	MLIM	750	0.6	dry	72	mean	0.10	0.02	1.45	5.93	6.87	0.67	1.60	0.77	0.34	0.25	0.41
						σ	0.02	0.01									
						n	41	41									
PM19	MLIM	725	0.4	10 % H2O	24	mean	0.11	0.01	1.53	3.65	5.29	0.72	2.10	0.64	0.33	0.19	0.48
						σ	0.03	0.01									
						n	22	20									
PM22	MLIM	725	0.4	10 % HF 4M	24	mean	1.12	0.03	1.57	4.20	5.63	0.60	2.09	0.86	0.28	0.28	0.44
						σ	0.10	0.01									
						n	6	12									
MF15C1	Preg/STAN	750	0.4	dry	72	mean	0.17	0.03	1.50	7.71	7.82	0.92	2.39	0.79	0.48	0.07	0.44
						σ	0.04	0.01									
						n	34	33									
MF15C2	Preg/PBT1	750	0.4	dry	72	mean	0.36	0.01	1.42	8.02	8.25	0.92	1.78	0.78	0.52	0.07	0.41
						σ	0.03	0.01									
						n	33	33									
MF15C3	Preg/PPL18	750	0.4	dry	72	mean	0.41	0.01	1.49	7.64	7.84	0.91	1.49	0.79	0.50	0.07	0.43
						σ	0.03	0.01									
						n	33	33									
MF15a	ASM/PBT1	750	0.4	dry	72	mean	0.47	0.01	1.64	7.00	7.34	0.91	1.79	0.88	0.48	0.07	0.45
						σ	0.02	0.01									
						n	26	26									
MF15b	ASM/STAN	750	0.4	dry	72	mean	0.27	0.03	1.64	7.52	7.68	0.91	2.54	0.84	0.48	0.08	0.44
						σ	0.04	0.01									
						n	19	19									
MF06a	PPL18/PPL18	700	0.4	dry	72	mean	0.41	0.01	1.83	6.91	7.20	0.79	1.35	0.76	0.42	0.17	0.40
						σ	0.02	0.01									
						n	23	23									
MF06b	PPL18/StAND	700	0.4	dry	72	mean	0.26	0.00	1.57	7.26	7.51	0.75	1.21	0.81	0.40	0.20	0.41
						σ	0.03	0.01									
						n	15	15									
FG8	glass SV0 /STAN	700	0.6	10 % HF 4M	8	mean	1.13	0.01	1.86	4.77	5.16	0.62	0.97	0.79	0.21	0.30	0.48
						σ	0.43	0.01									
						n	29	29									

This is the peer-reviewed, final accepted version for American Mineralogist, published by the Mineralogical Society of America.
The published version is subject to change. Cite as Authors (Year) Title. American Mineralogist, in press.
DOI: https://doi.org/10.2138/am-2022-8663. http://www.minsocam.org/

TABLE 4. EMPA of biotite from PPL18 and MLIM, before and after the experimental runs, and the obtained concentration ratios sm/exp; exp – experiment; sm – starting material. Biotite end-members and IV(F) calculated according to Munoz (1984).

sample		F	Cl	XMg	Xsid	Xan	IV(F)
PPL18 sm	mean	2.28	0.01	0.42	0.41	0.17	1.21
n = 82	σ	0.19	0.00				
PPL18 exp	mean	2.40	0.01	0.41	0.41	0.18	1.17
n = 130	σ	0.28	0.01				
	sm/exp	1.05	1.0	0.98	1.0	1.06	0.97
MLIM sm	mean	0.30	0.05	0.40	0.48	0.12	2.18
n = 21	σ	0.08	0.00				
MLIM exp	mean	0.31	0.05	0.40	0.48	0.12	2.16
n = 78	σ	0.02	0.00				
	sm/exp	1.03	1.0	1.0	1.0	1.0	0.99

TABLE 5. Experimental anatexis conditions and EPMA of experimentally neo-formed biotite.

Run	T (°C)	P (GPa)	fluid	hours	sample		F	Cl	XMg	Xsid	Xan	IV(F)	log(f H_2O/f HF)
PM22	930	6	dry	24	MLIM	mean	0.44	0.06	0.44	0.41	0.15	2.06	3.81
					n = 8	σ	0.04	0.00					
PM22	725	4	HF 4M	24	MLIM	mean	2.49	0.01	0.41	0.43	0.17	1.14	3.24
					n = 6	σ	0.22	0.00					
PM20	930	6	dry	24	PPL18	mean	3.10	0.01	0.51	0.36	0.14	1.12	2.87
					n = 5	σ	0.38	0.00					
MF15C	750	4	dry	72	PPL18	mean	1.70	0.01	0.31	0.62	0.07	1.21	3.26
					n = 5	σ	0.08	0.01					
MF17B	725	4	HF 4M	24	PPL18	mean	5.08	0.01	0.34	0.56	0.11	0.46	2.57
					n = 6	σ	0.09	0.01					
MF06	700	4	dry	72	PPL18/St	mean	0.59	0.02	0.36	0.52	0.12	1.81	3.97
					n = 10	σ	0.09	0.00					
FG8	700	6	HF 4M	8	SV0+Bt	mean	2.20	0.13	0.30	0.46	0.17	1.17	3.32
					n = 5	σ	0.06	0.01					

This is the peer-reviewed, final accepted version for American Mineralogist, published by the Mineralogical Society of America.
The published version is subject to change. Cite as Authors (Year) Title. American Mineralogist, in press.
DOI: https://doi.org/10.2138/am-2022-8663. http://www.minsocam.org/

TABLE 6. EPMA of F and related IV(F) values (Munoz, 1984) of co-existing biotite and muscovite. The mica pairs come from regional profiles across the de Seridó belt and from the contact with granitic intrusions for the Seridó schist and Jucurutu gneiss. Other pairs are from the Acari pluton sheared granite (Sallet et al. 2018), and from the Serra Verde pegmatitic granite (Sallet et al. 2018, 2021).

sample	rock	F(Bt)	F(Ms)	F(Bt)/F(Ms)	IV(F)Bt	IV(F)Mus	ratio
PAJ8	regional schist	0.38	0.13	2.9	2.02	1.80	1.1
PPP8	regional schist	0.37	0.13	2.8	2.01	1.81	1.1
2M	regional schist	0.38	0.14	2.7	2.09	1.84	1.1
1M	regional schist	0.39	0.15	2.6	2.08	1.82	1.1
Pt35	regional schist	0.33	0.13	2.5	2.06	1.80	1.1
PPL18	contact schist	2.49	0.76	3.3	1.24	1.07	1.2
PCNW4	contact schist	1.05	0.31	3.4	1.58	1.47	1.1
PCNW 6	contact schist	1.06	0.31	3.4	1.57	1.47	1.1
MAR AX	contact schist	0.69	0.26	2.7	1.64	1.57	1.0
MAR A2a	contact schist	0.48	0.16	3.0	1.93	1.72	1.1
MAR A2b	contact schist	0.49	0.16	3.1	1.81	1.73	1.0
MLIM	contact schist	0.30	0.12	2.5	2.19	1.86	1.2
J23	regional gneiss	0.39	0.17	2.3	2.08	1.82	1.1
J19	regional gneiss	0.41	0.17	2.4	2.07	1.83	1.1
J28	regional gneiss	0.40	0.17	2.4	2.10	1.83	1.1
94.1	contact gneiss	0.75	0.27	2.8	1.79	1.64	1.1
94.2	contact gneiss	0.86	0.27	3.2	1.83	1.67	1.1
94.3	contact gneiss	0.44	0.17	2.6	2.09	1.85	1.1
94.4	contact gneiss	0.35	0.17	2.1	2.17	1.85	1.2
94.5	contact gneiss	0.31	0.15	2.1	2.19	1.90	1.2
Pt60A	sheared granite	0.69	0.26	2.7	1.64	1.51	1.1
Pt63	sheared granite	0.98	0.48	2.0	1.52	1.32	1.2
Pt64	sheared granite	0.64	0.16	4.0	1.85	1.69	1.1
SV	pegmatitic granite	0.98	0.50	2.0	1.38	1.21	1.1
average				**2.7**			**1.1**
σ				0.50			0.04
n = 24							

TABLE 7. Composition of the experiment after the runs obtained by combining BSE image analysis and mass balance procedures between the composition of the starting material and run products.

MF15	wt%	Mus	Melt	Bt 1	Kf	Als	Q	Bt 2	Total
PReg/PBT1		4.0	17.9	51	4.00	10.2	6.0	6.9	100
PReg/PPL18		4.0	16.1	51	4.00	10.4	8.1	6.4	100
PReg/STAN		4.0	15.9	51	4.00	11.5	7.1	6.5	100
ASM/PBT1		4.0	14.5	51	4.00	11.0	8.3	7.2	100
ASM/STAN		4.0	16.1	51	4.00	10.4	8.1	6.4	100
	avg	**4.0**	**16.1**	**51**	**4.0**	**10.7**	**7.5**	**6.7**	
	σ	0.0	1.2	0.0	0.0	0.5	1.0	0.4	

This is the peer-reviewed, final accepted version for American Mineralogist, published by the Mineralogical Society of America.
The published version is subject to change. Cite as Authors (Year) Title. American Mineralogist, in press.
DOI: https://doi.org/10.2138/am-2022-8663. http://www.minsocam.org/

TABLE 8. Experimental biotite-melt F partition coefficients, $Kd_{(F)} = (F)_{Bt} / (F)_{melt.}$

run	sample	SM	T (°C)	GPa	hours	fluid	F bt	F melt	Kd (bt/mlt)	MgO bt
PM20	PPL18	rock	930	0.6	24	dry	3.1	0.55	5.64	14.59
PM22	PPL18	rock	725	0.4	24	10 % HF 4N	5.1	2.72	1.88	8.75
MF15C1	PegReg/PPL18	synt.xist	750	0.4	72	dry	1.6	0.41	3.90	7.91
MF06	PPL18/StAnd	synt.xist	700	0.4	72	dry	0.59	0.26	2.27	9.09
MF17B	MLIMP	rock	930	0.6	24	dry	0.44	0.13	3.38	11.71
PM22	MLIMP	rock	725	0.4	24	10 % HF 4N	2.49	1.12	2.22	10.70
FG8	SVC+Bt	synt.glass	700	0.6	8	10 % HF 4N	2.2	1.11	1.98	8.72
avg (n = 7)									**3.04**	
σ									**1.38**	

This is the peer-reviewed, final accepted version for American Mineralogist, published by the Mineralogical Society of America.
The published version is subject to change. Cite as Authors (Year) Title. American Mineralogist, in press.
DOI: https://doi.org/10.2138/am-2022-8663. http://www.minsocam.org/

Figure 01

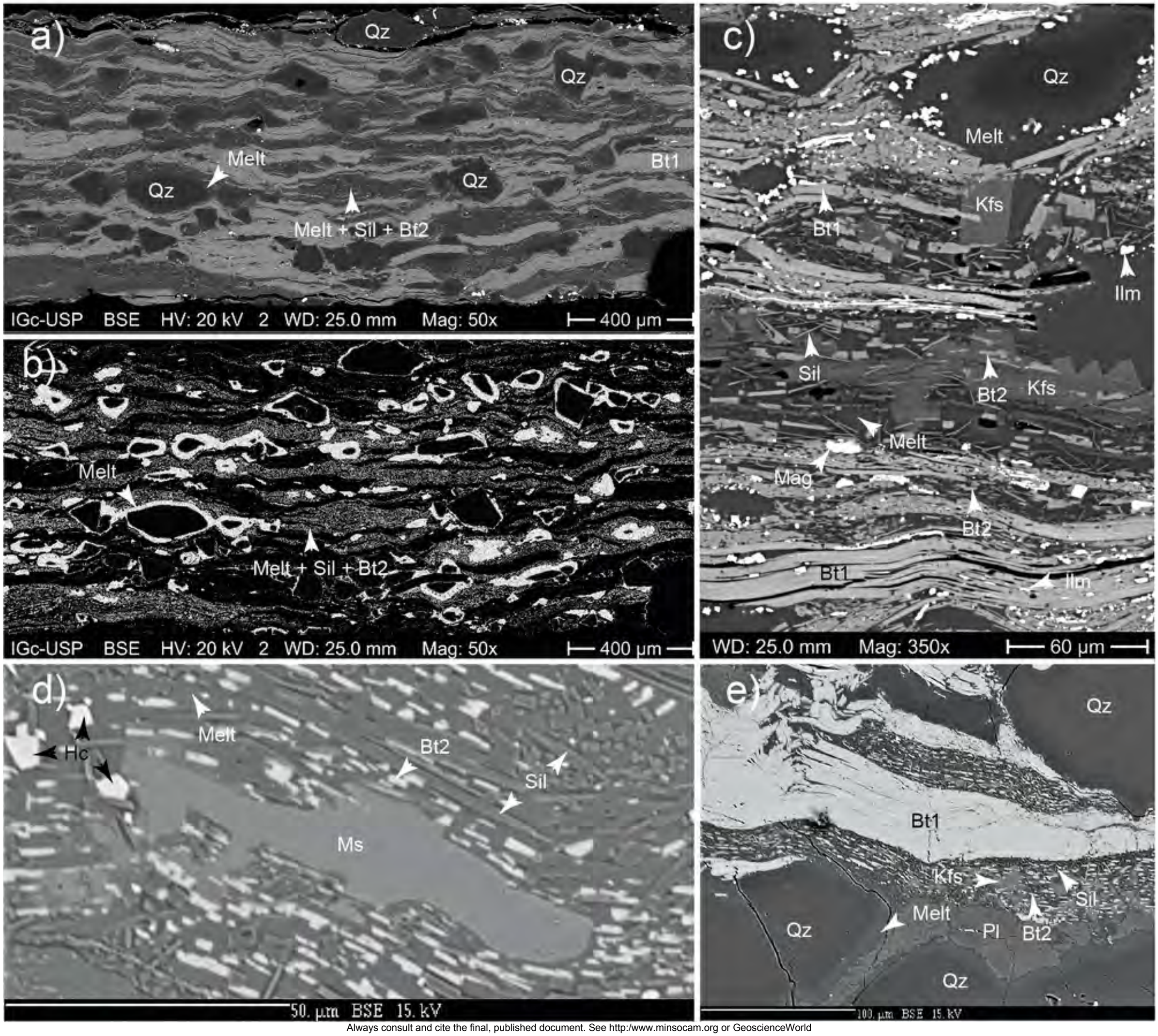

Figure 02

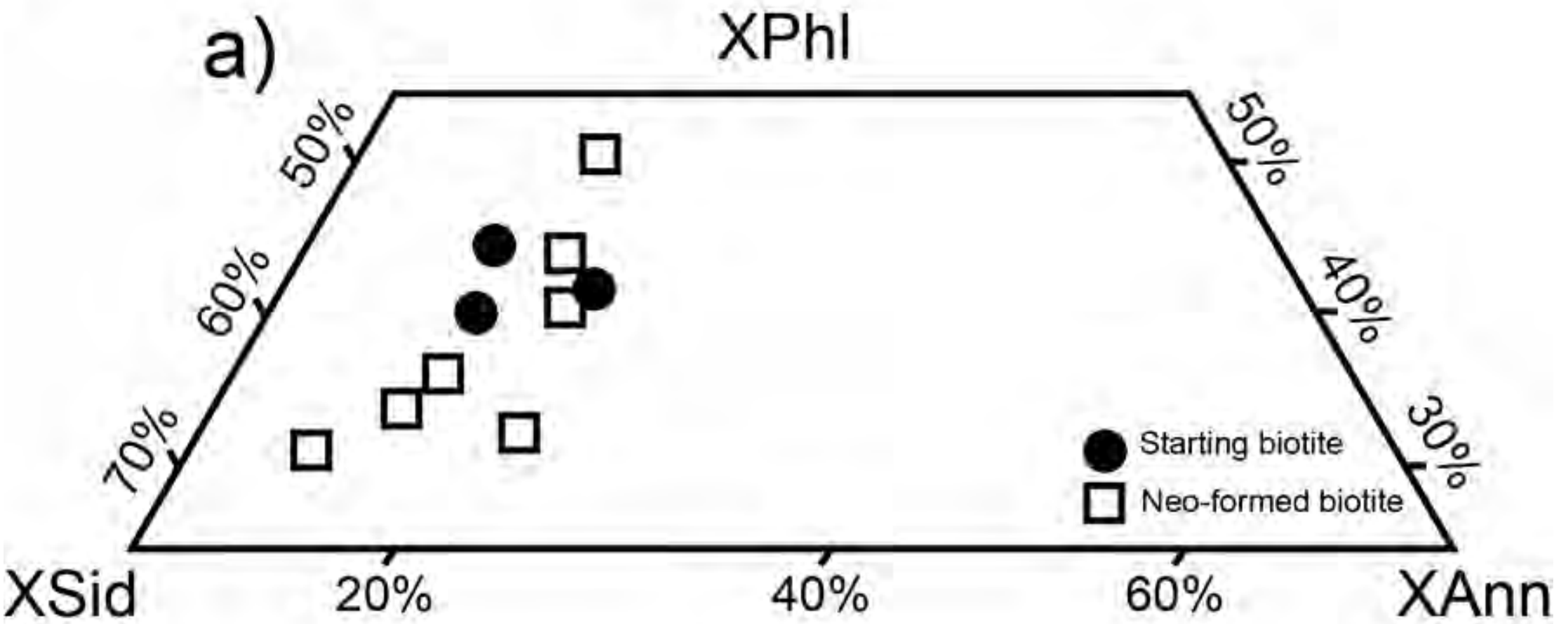

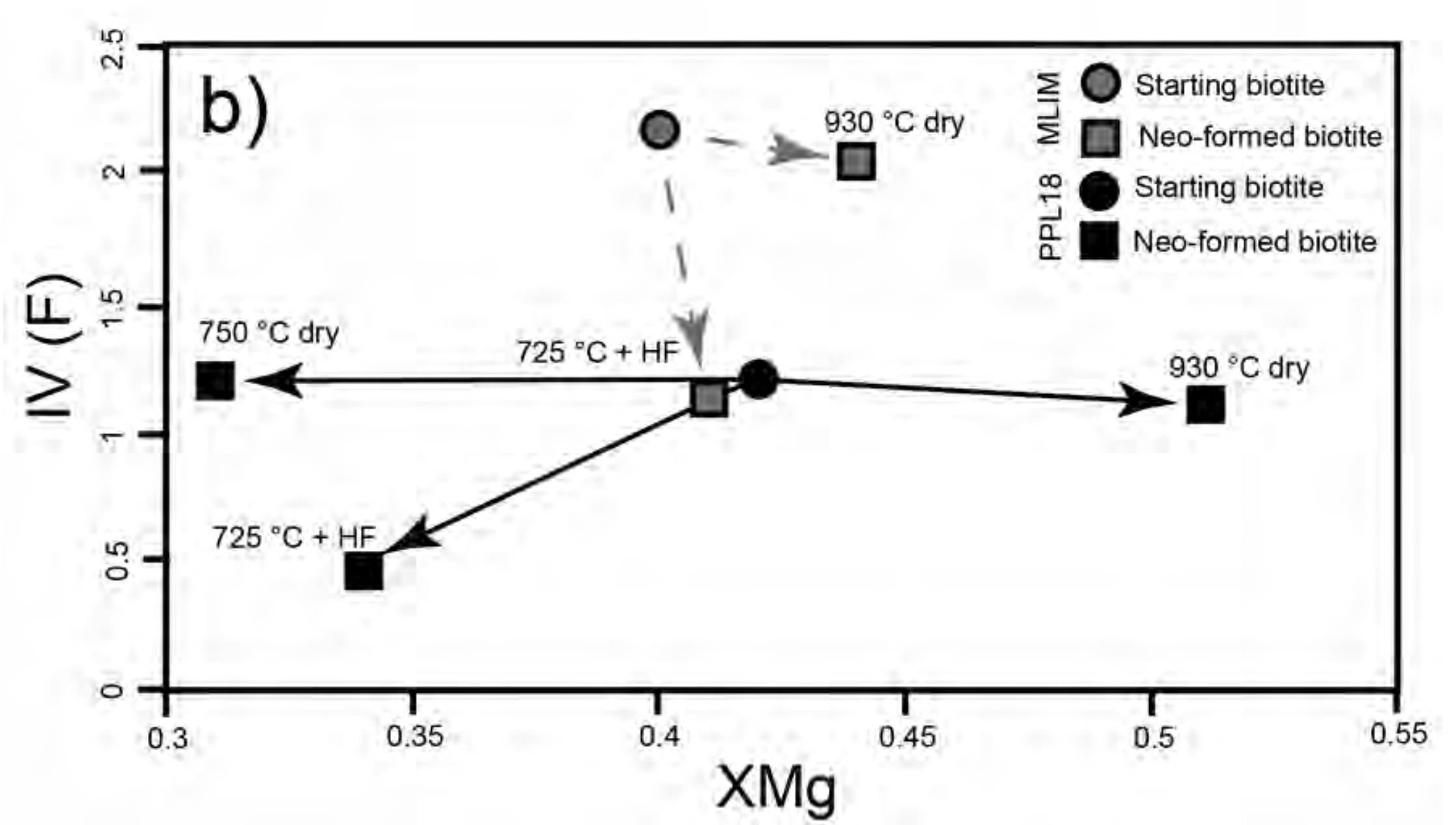

Figure 03

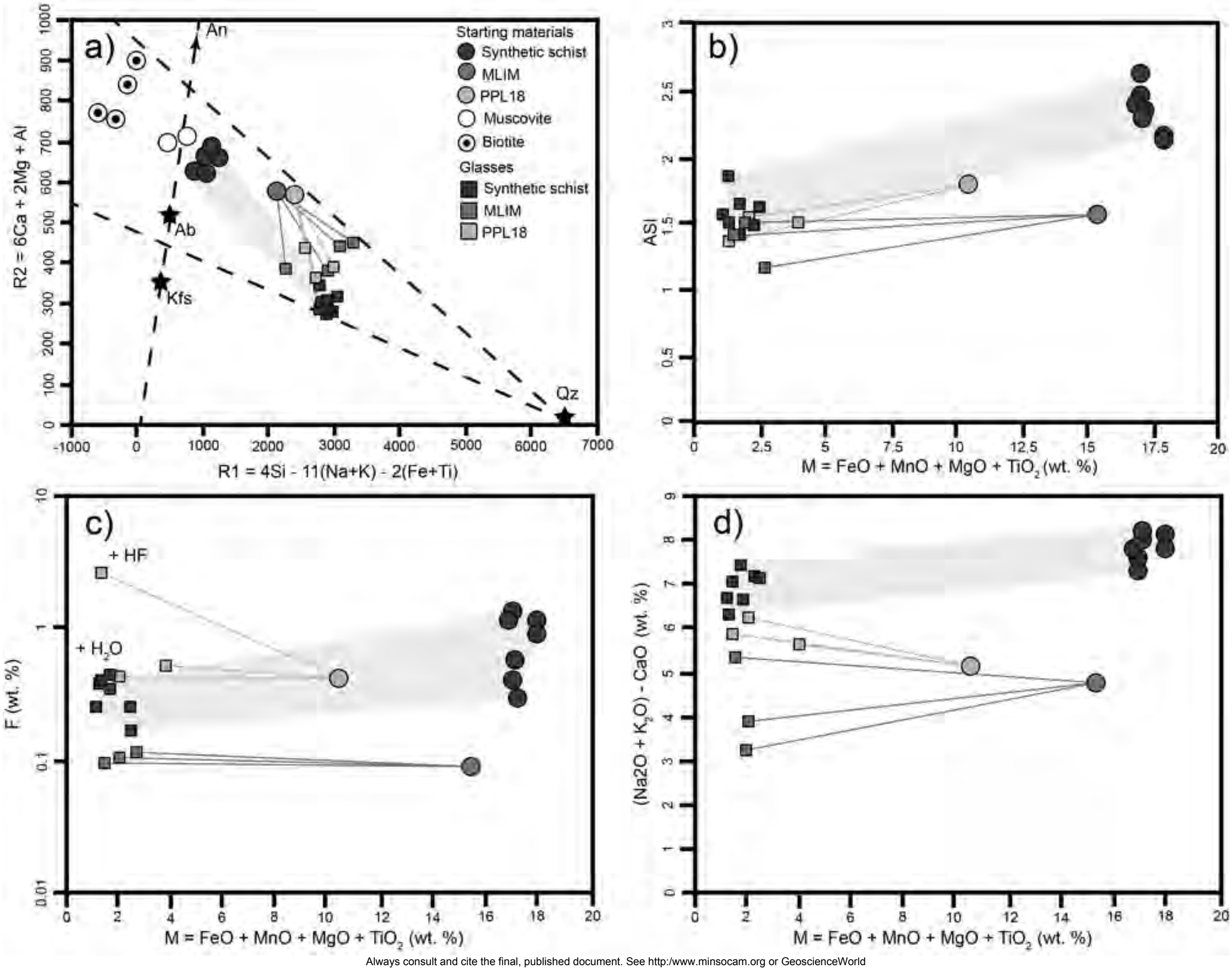

Figure 04

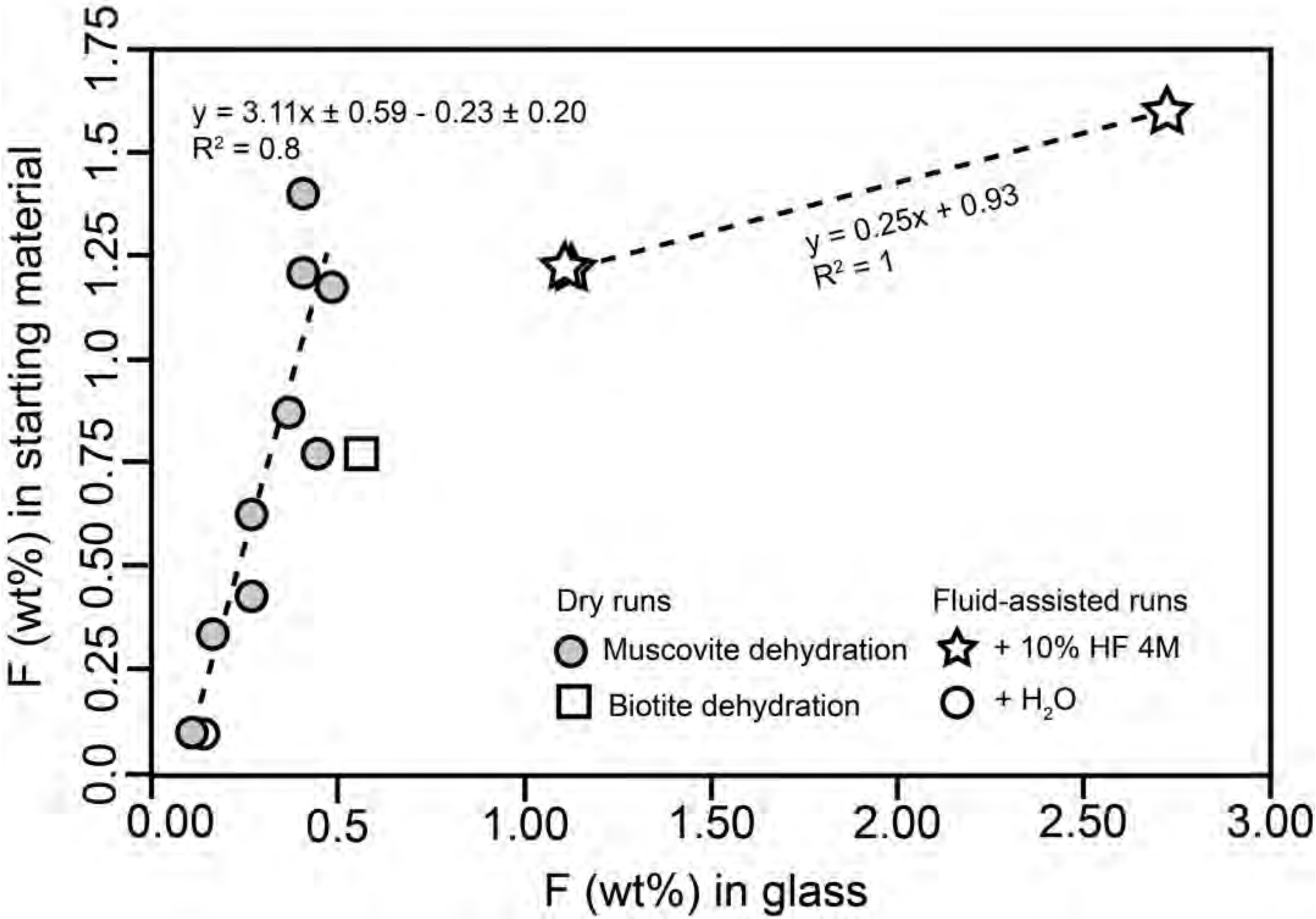

Figure 05

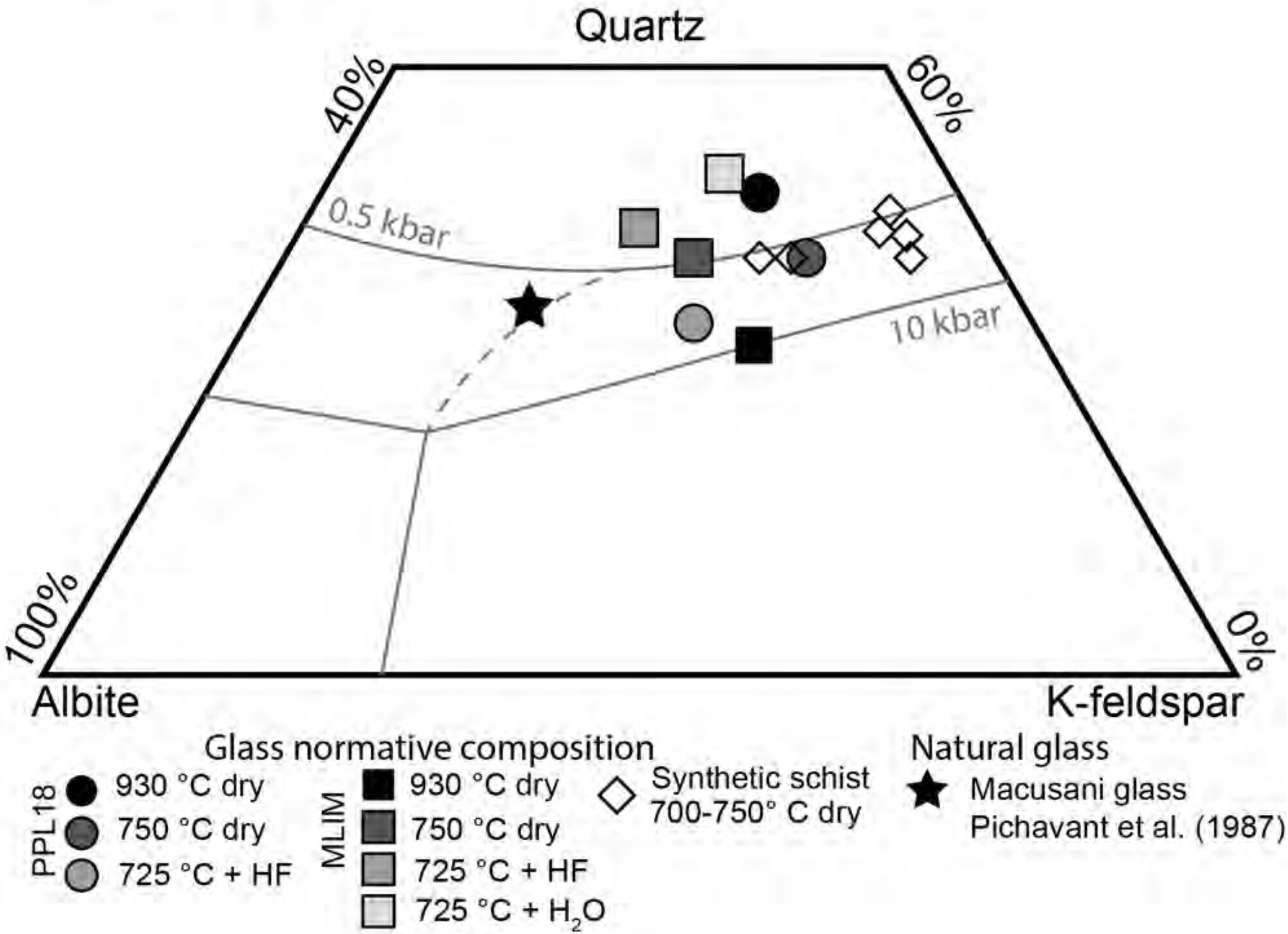

Figure 06

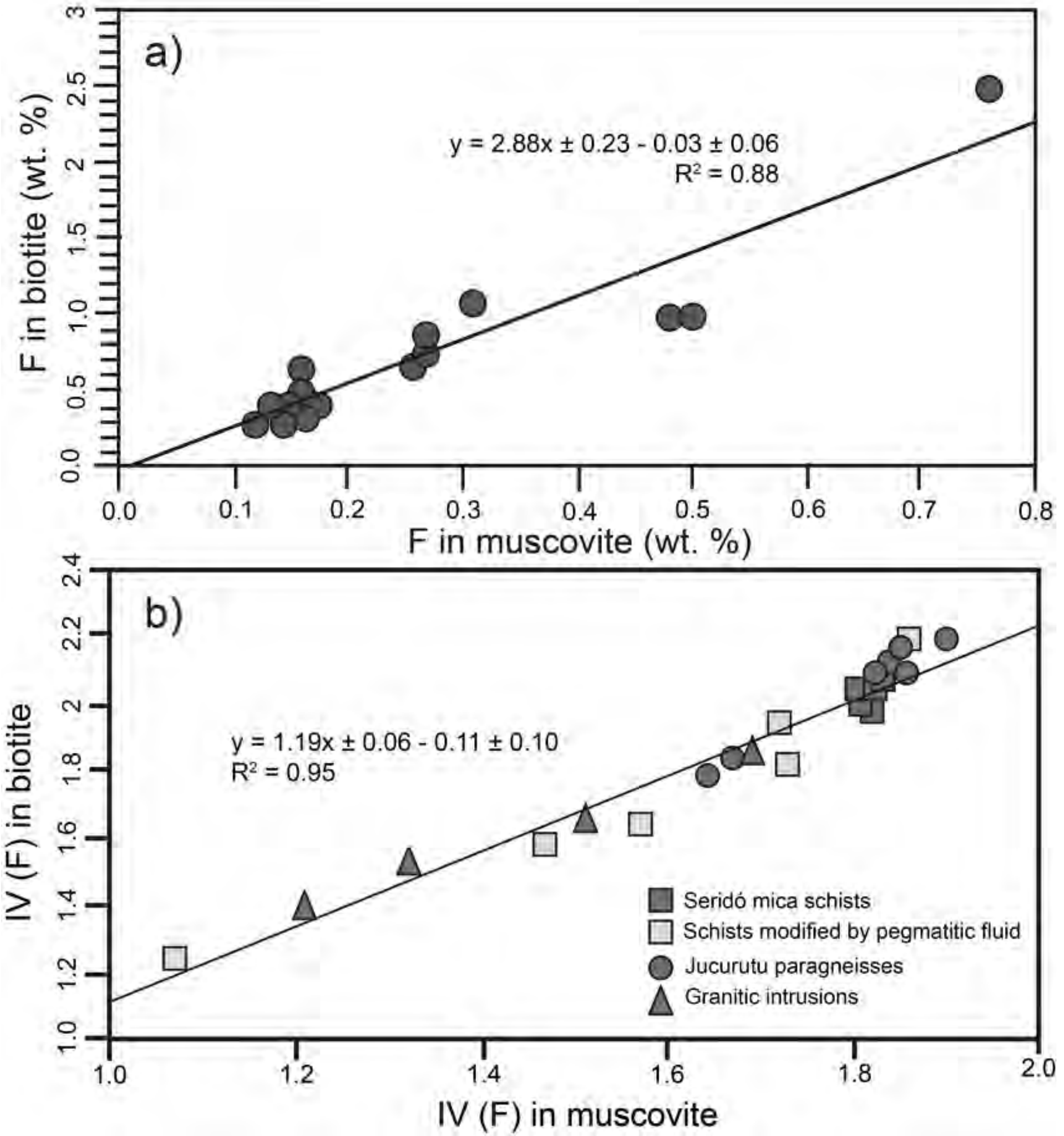

Figure 07

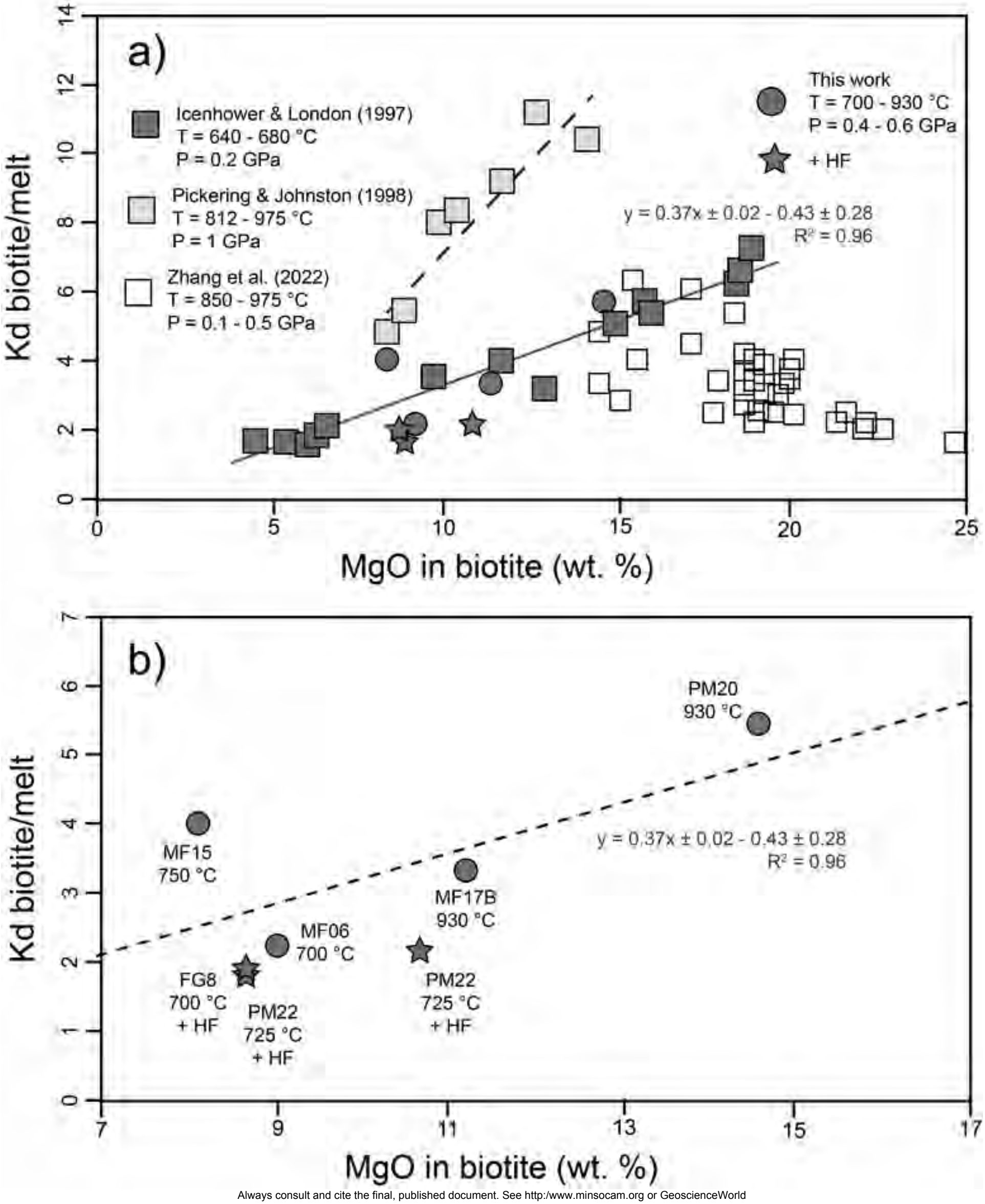

Figure 08

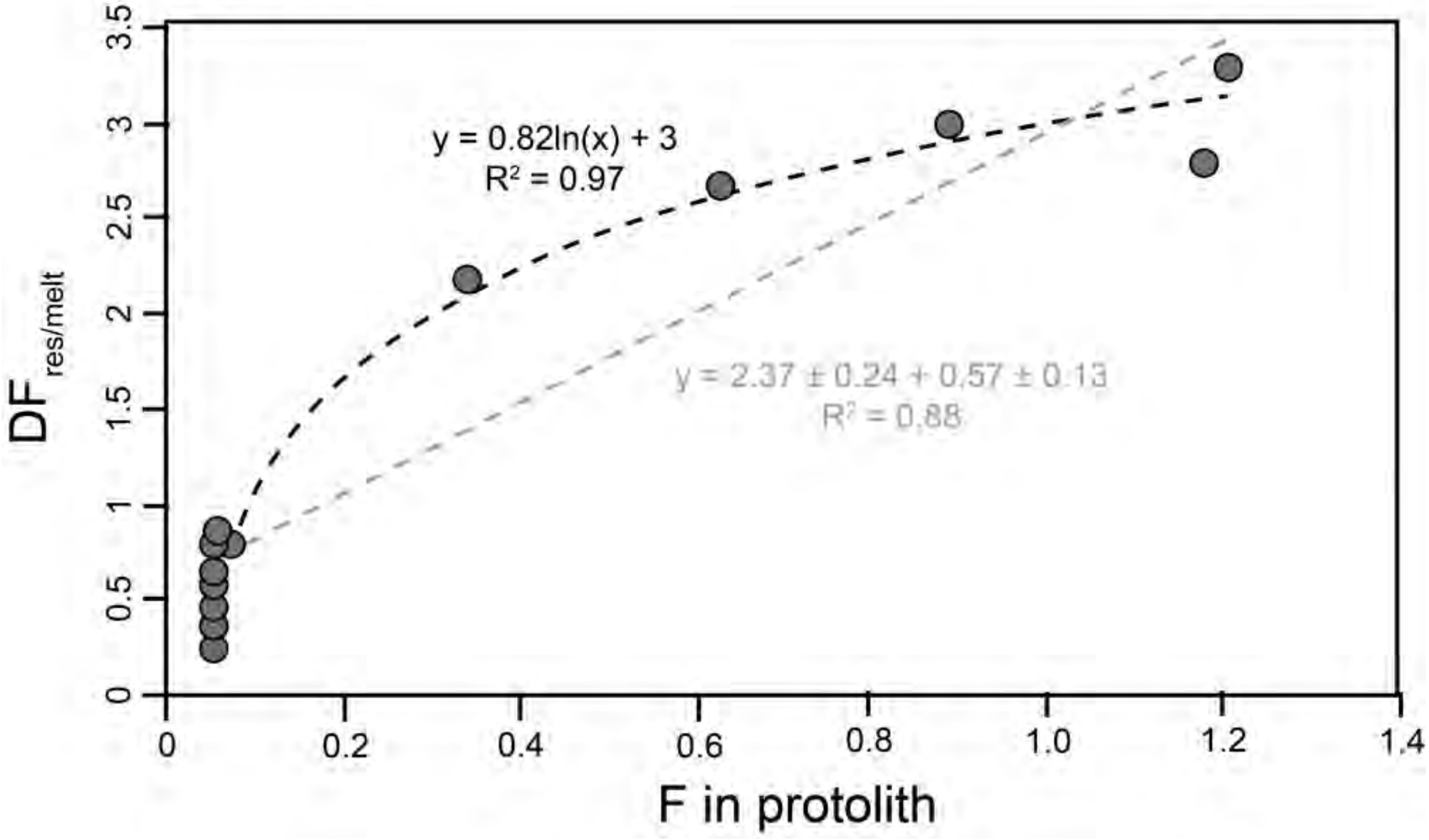

Figure 09